

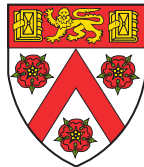
PART II

---

Computation of horizontally invariant nonlinear  
solutions in an eccentric shearing box

---

Aaron WIENKERS



TRINITY COLLEGE  
UNIVERSITY OF CAMBRIDGE

March 2016

# Contents

<b>1</b>	<b>Introduction</b>	<b>1</b>
<b>2</b>	<b>Mathematical Model</b>	<b>1</b>
2.1	Global Disc Dynamics . . . . .	1
2.2	Shearing Box Approximation . . . . .	2
2.3	Semi-Analytic Solution . . . . .	3
<b>3</b>	<b>Numerical Method</b>	<b>5</b>
3.1	Boundary Conditions . . . . .	6
3.2	Initial Conditions . . . . .	6
<b>4</b>	<b>Results and Validation</b>	<b>7</b>
<b>5</b>	<b>Conclusions and Future Work</b>	<b>9</b>

### **Abstract**

The shearing box approximation to the compressible Euler equations modelling shearing, rotating, and stratified flows in a local frame is presented in a generalised form for eccentric discs. A semi-analytic solution describing the nonlinear laminar vertical resonant solutions to this model is found for the special case of an isothermal disc. The overall 2<sup>nd</sup> order finite volume method constructed and validated in Part I of this series is modified to solve for the oscillatory geometric source terms arising from the eccentric orbit. This modified algorithm based on the well-balanced MUSCL TVD scheme using the HLLC approximate Riemann solver is employed to solve for the 1D horizontally invariant laminar solutions first identified in Ogilvie (2001). The finite volume implementation is consequently validated against the known semi-analytic isothermal solutions for a range of disc eccentricities.

# 1 Introduction

Razor thin viscous circular accretion discs have been well studied since the early seminal theory of Pringle (1981). Much of this attention has been focused on searching for instabilities with efficient modes of mass and angular momentum transport through the disc. Yet there are no widely accepted local purely hydrodynamic instabilities in cylindrical discs efficient enough to explain the deduced rate of mass accretion through observable discs. Thus by lifting the assumption of a cylindrical disc, additional instability and transport processes may be excited.

Although the lowest orbital energy state is circular, Syer and Clarke (1992) have shown that not every disc tends to circularise, breaking a fundamental assumption in early disc theory. Indeed, Lin and Pringle (1976) have shown that circularisation is inevitable for the special case of discs in a binary potential; however, in general this is dependent on the phase of the stresses in relation to the orbital phase. Analogous to the classic axisymmetric orbital diffusion problem for a circular ring, Syer and Clarke evolved an elliptical ring of matter, finding that the initial eccentricity can be sustained even on viscous timescales for aligned orbits of similar eccentricities. Additional mechanisms have more recently been found to couple with the evolution of eccentric disc modes and continually perturb or sustain eccentric orbits. These eccentric perturbations may be related to the origination of the disc, due to the continuous anisotropic mass transfer from a binary companion Roche overflow (Whitehurst, 1988) or from the parent nebular cloud core. This close binary companion may also couple to the eccentric modes in the disc and support resonances producing exponentially growing eccentricities (Lubow, 1991, 2010). Eccentricity can also be sustained by a viscous instability to eccentric perturbations which is known to exist for particular viscosity prescriptions, including the often-used  $\alpha$ -viscosity (Lyubarskij et al., 1994). Finally, secular interactions with embedded planets (as would be present in the nascence of protoplanetary disc development) have been theoretically and numerically shown to induce eccentricity in discs (Papaloizou, 2005; Kley and Dirksen, 2006).

Thus the classical theory of accretion discs (Pringle, 1981) has been generalised to accommodate this additional degree of freedom in the orbital energy (Ogilvie, 2001). Eccentric discs store additional energy in the first azimuthal orbital mode, which opens up possibilities for instability and energy extraction not available to cylindrical discs. One such mode arises from the parametric coupling between the eccentric azimuthal mode and vertical oscillations inherent to eccentric discs, generating inertial waves capable of transporting mass and angular momentum (Papaloizou, 2005; Barker and Ogilvie, 2014). These vertical resonant oscillations arising from the disc eccentricity will be the primary focus in this paper.

## 2 Mathematical Model

### 2.1 Global Disc Dynamics

A global hydrodynamical model of a general accretion disc may be realised by simply adding a gravitational term,  $\nabla\Phi_g$ , to the Euler equations. For a non-self-gravitating Keplerian disc, the point mass potential is  $\Phi_g = -GM/\sqrt{r^2 + z^2}$  at a radius  $r$  and vertically offset from the disc midplane by  $z$ . The initial orbital energy and angular momentum of a fluid parcel uniquely determines the eccentricity of the orbit. Consider a fluid parcel initially located at  $r = \lambda$  with a specific orbital angular momentum  $\ell = \sqrt{GM}\lambda$ . Given a specific orbital energy equal to  $E = -GM/(2\lambda)$ , the fluid particle will take on a circular orbit; however, if the energy is increased to  $E = -(1 - e^2)GM/(2\lambda)$ , the orbit becomes eccentric with eccentricity  $e$ . Thus a particular orbit is uniquely defined by the semi-latus rectum,  $\lambda$ , along with the orbit eccentricity. The natural disc coordinate system  $(\lambda, \phi)$  therefore can describe any point in the disc when the eccentricity,  $e(\lambda)$ , and the longitude of pericentre,  $\omega(\lambda)$ , are also specified, and which are in general functions of  $\lambda$ . This will make it possible to map the global coordinates,  $(\lambda, \phi, z)$ , into a local co-orbiting coordinate system,  $(\xi, \eta, z)$ , centred at  $(\lambda_0, \varphi(t), 0)$  in the eccentric disc, as shown in Figure 1. The Jacobian for this coordinate transformation from cartesian into the

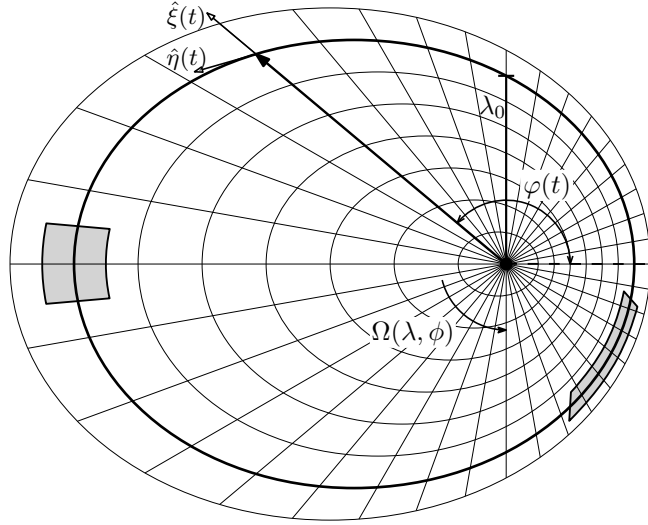


Figure 1: The global orbital coordinate grid,  $(\lambda, \phi)$ , shown overlaid on the disc. The fiducial orbit,  $\lambda_0$ , is shown in bold along with the local horizontal coordinates  $(\xi, \eta)$ . The initial shearing box control volume at apocentre is shown sheared, stretched, and advected at a later time.

eccentric orbital coordinates is

$$J(\lambda, \phi, z) = \frac{\partial(x, y, z)}{\partial(\lambda, \phi, z)} = \frac{\lambda(1 + (e - \lambda e') \cos \theta - \lambda e \omega' \sin \theta)}{(1 + e \cos \theta)^3} \quad (1)$$

where  $e'$  and  $\omega'$  are the eccentricity gradient and orbital phase shift (or disc twistedness), respectively.  $\theta = \phi - \omega$  here is the true anomaly, measuring the angular distance from pericentre.

## 2.2 Shearing Box Approximation

For studying *local* small-scale phenomena, it is numerically and analytically beneficial to enter a local reference frame co-orbiting and shearing with the disc. The non-axisymmetric geometry makes the formulation conceptually more difficult, and so it will be easier to start with the vertical terms in the local cylindrical disc shearing box developed in Part I of this series. The governing equations in the local cartesian coordinates,  $(x, y, z) = (r - R_0, R_0(\phi - \phi_0 - \Omega_0 t), z)$ , centred about a fiducial radius,  $R_0$ , and co-rotating with the orbital frequency,  $\Omega_0$ , are

$$\frac{D\rho}{Dt} = -\rho \frac{dw}{dz} \quad (2a)$$

$$\frac{Dw}{Dt} = -\frac{1}{\rho} \frac{dp}{dz} - \frac{d\Phi_2}{dz} \quad (2b)$$

$$\frac{De}{Dt} = -\frac{p}{\rho} \frac{dw}{dz}, \quad (2c)$$

where  $\Phi_2 = \frac{1}{2}z^2GM/R_0^3$  is the second order term in the expansion of the effective tidal potential, and  $\frac{D}{Dt}(\cdot)$  is the total (Lagrangian) derivative. An ideal gas equation of state,  $p = (\gamma - 1)e$ , is again used to provide closure. The solutions to this system of equations are horizontally invariant in this local frame because each of the terms are independent of the local horizontal coordinates,  $x$  and  $y$ .

An analogous expansion can be made for an eccentric disc in the local coordinates,  $(\xi, \eta, z) = (\lambda - \lambda_0, \phi - \varphi(t), z)$ , which are co-orbiting about a fiducial orbit,  $\lambda_0$ , centred on the midplane at  $\phi = \varphi(t)$ , and rotating with the disc at orbital frequency  $\Omega(\lambda_0, \phi)$ . Two additional terms arise in (2) when considering the eccentricity. First, it is apparent that the effective tidal potential

expansion now varies with  $\phi$ . Expanding the tidal potential similarly to the cylindrical case, but with  $R(\theta) = \lambda_0/(1 + e \cos \theta)$ , the second order term which appears in the shearing box approximation is

$$\Phi_2 = \frac{GM}{\lambda_0^3} (1 + e \cos \theta)^3, \quad (3)$$

which is an implicit function of  $t$ , periodic with the eccentric orbital period,

$$\mathcal{P} = 2\pi \sqrt{\frac{\lambda_0^3}{GM}} (1 - e^2)^{-3/2}. \quad (4)$$

This is a periodic variation in the vertical gravitational acceleration due to the time-varying radius while on a constant orbit,  $\lambda_0$ .

A second modification to the cylindrical shearing box originates in the oscillatory geometry of the disc. Although the vertical ( $\hat{\mathbf{z}}$ ) direction remains unchanged in the transformation, each of the velocity divergence terms in (2a) and (2c) must be transformed into the new coordinate system, and are non-zero due to the azimuthal velocity of the fiducial orbit,  $d\varphi/dt = \Omega$ . Accounting for this horizontal velocity divergence amounts to including an additional energy and mass source to the governing equations. Using the Jacobian,  $J(\lambda_0, \phi, 0)$ , for the eccentric orbital coordinates, this velocity divergence on the  $\lambda_0$  orbit can be expressed as

$$\Delta = \frac{1}{J} \frac{\partial}{\partial \phi} (J\Omega) = \sqrt{\frac{GM}{\lambda_0^3}} \frac{\lambda_0(1 + e \cos \theta) (e' \sin \theta - e\omega'(\cos \theta + e))}{1 + (e - \lambda_0 e') \cos \theta - \lambda_0 e \omega' \sin \theta}. \quad (5)$$

This is again an implicit periodic function of time, with period  $\mathcal{P}$ , which arises from the misalignment of the apse lines in the disc ( $\omega'$ ) in addition to the non-constant eccentricity ( $e'$ ).

Thus the modified vertical governing equations in the eccentric shearing sheet are

$$\frac{D\rho}{Dt} = -\rho \frac{\partial w}{\partial z} - \rho \Delta \quad (6a)$$

$$\frac{Dw}{Dt} = -\frac{1}{\rho} \frac{\partial p}{\partial z} - \Phi_2 z \quad (6b)$$

$$\frac{Dp}{Dt} = -\gamma p \frac{\partial w}{\partial z} - \gamma p \Delta, \quad (6c)$$

The full 3D eccentric shearing box equations are presented in Ogilvie and Barker (2014), by additionally transforming the local horizontal coordinates,  $\xi$  and  $\eta$ . The result is a shearing box on orbit  $\lambda_0$ , both shearing and periodically stretching azimuthally. Figure 1 shows this large orbital convergence near pericentre, as well as the azimuthal elongation of a shearing box between apocentre and just before pericentre due to the relative azimuthal acceleration of points on the same orbit.

### 2.3 Semi-Analytic Solution

A naïve quasi-hydrostatic approach to solving the 1D system (6) might involve finding the isothermal scale height for a cylindrical disc at radius  $R(\theta) = \lambda_0/(1 + e \cos \theta)$  as it varies about the orbit. Although incorrect due to neglecting all dynamics of the system, it is still instructive for demonstrating the resonant amplification (shown in Figure 2 for a disc with  $e = 0.3$ ).

A semi-analytic solution to the 1D system (6) becomes possible after noticing the eccentric periodic forcing terms generate homogeneous vertical oscillations. Isothermal thermodynamics will also be assumed for the following analysis; however, Ogilvie and Barker (2014) present the theory for general thermodynamics. The primitive variables are rewritten to uncouple the temporal and spatial dependencies by exploiting the solution form of the homogeneous oscillations,

$$\rho(t, z) = \hat{\rho}(t) e^{-\zeta^2/2} \quad (7a)$$

$$w(t, z) = \hat{w}(t) z \quad (7b)$$

$$p(t, z) = \hat{p}(t) e^{-\zeta^2/2} \quad (7c)$$

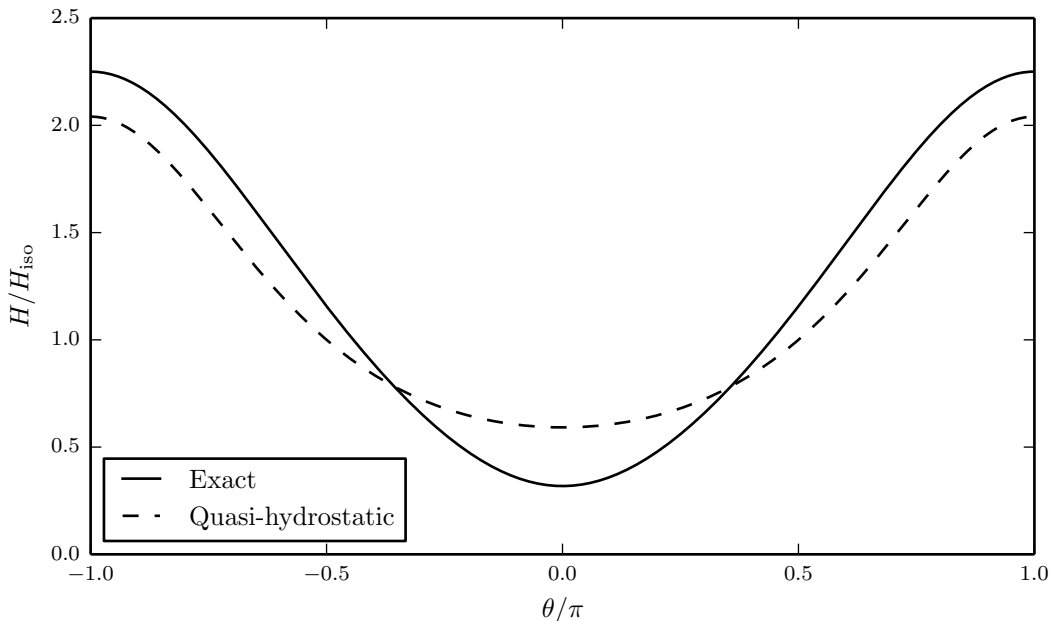


Figure 2: Comparison of the resonant solution with the naïve solution which uses the hydrostatic scale height at each orbital radius, for  $e = 0.3$ .

where the similarity variable,  $\zeta(t) = z/H(t)$ , can be defined for an isothermal disc. The governing equations are then uncoupled by inserting this form for the primitive variables into (6):

$$\frac{\dot{\hat{\rho}}}{\hat{\rho}} - \frac{H}{\hat{H}}\zeta^2 - \hat{w}\zeta^2 = -(\Delta + \hat{w}) \quad (8a)$$

$$\dot{\hat{w}} + \hat{w}^2 = -\Phi_2 + \frac{c_s^2}{H^2}, \quad (8b)$$

where the redundant pressure equation is dropped. However, since the additional variable  $H(t)$  has been introduced, a final relation is needed to close the system. This is found using a global mass conservation argument motivated by the mass component (6a). Integrating this term vertically over the disc, and using the form (7a), the closing equation is

$$\frac{\dot{\hat{\rho}}}{\hat{\rho}} + \frac{\dot{H}}{H} = -\Delta. \quad (9)$$

This set now can be simplified in terms of  $H$ , giving a second order non-linear ODE describing the evolution of  $H$ :

$$\ddot{H} = -\Phi_2 H + \frac{c_s^2}{H}. \quad (10)$$

This ODE describes a non-linear oscillator periodically forced by  $\Phi_2$ . Just as with any oscillator, this ODE admits both free oscillations as well as the forced response driven at the orbital frequency. The purely forced response can then be obtained by writing this as a periodic boundary value problem that can be solved numerically for  $H$ , and for which  $\hat{\rho}$ ,  $\hat{w}$ , and  $\hat{p}$  easily follow.

Thus an eccentric disc exhibits a vertical oscillatory “breathing” mode, where the disc scale height periodically expands and contracts. Figure 3 shows the vertical disc profile exhibiting this oscillation with equally spaced snapshots in time, starting (from the bottom) at apocentre, and displaying a large thin compression at pericentre. It is this vertical oscillation mode that parametrically couples with the orbital frequency and produces the inertial waves described in Papaloizou (2005).

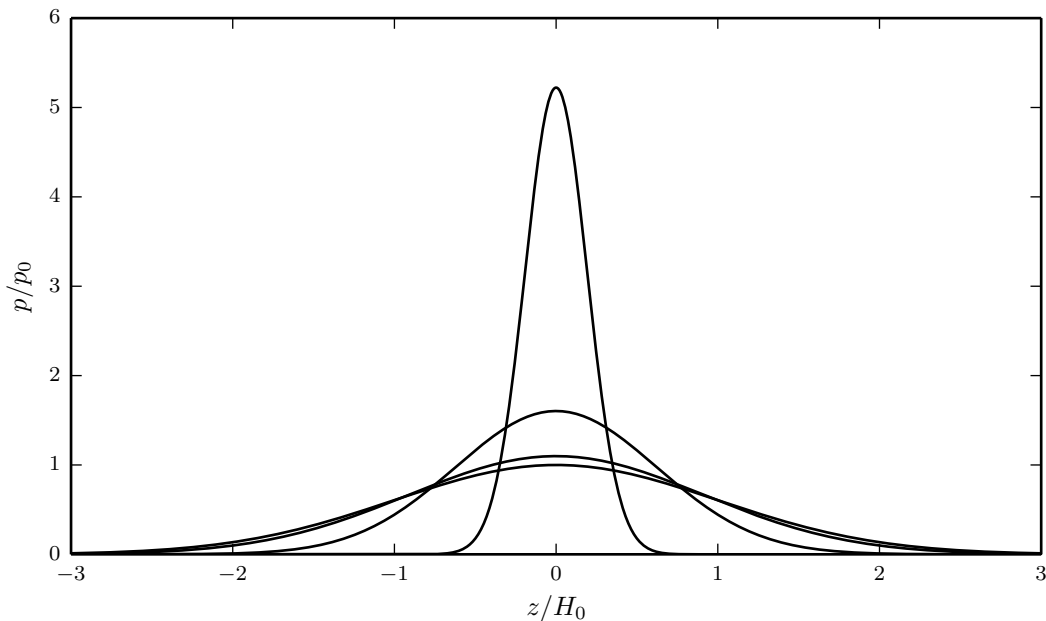


Figure 3: Equally spaced snapshots in time with  $\Delta t = \mathcal{P}/6$ , between pericentre (top) and apocentre (bottom) for a disc with  $e = 0.3$ .

### 3 Numerical Method

The finite volume method is employed to numerically solve the model described by the system of equations (6) cast in conservative form:

$$\frac{\partial}{\partial t} \begin{pmatrix} \rho \\ \rho w \\ E \end{pmatrix} + \frac{\partial}{\partial z} \begin{pmatrix} \rho w \\ \rho w^2 + p \\ (E + p)w \end{pmatrix} = \begin{pmatrix} -\rho\Delta \\ -\rho w\Delta - \Phi_2\rho z \\ -(E + p)\Delta - \Phi_2\rho w z \end{pmatrix} \quad (11)$$

where each  $\Delta$  and  $\Phi_2$  are periodic in time. The vector of conserved variables  $\mathbf{U} = (\rho, \rho w, E)^T$  is marched forward in time in an unsplit fashion, integrating both the hyperbolic advection flux on the left hand side in parallel with the source term,  $\mathbf{S}(\mathbf{U}, t)$ , on the right side. To match the assumptions made in the semi-analytic solution derived in §2.3, the ratio of specific heats,  $\gamma$ , is set equal to 1.00001 to emulate an isothermal equation of state. This is a common trick to reduce a compressible implementation solving for the internal energy into one where the internal energy varies directly with density as for an isothermal fluid. It amounts to defining many internal degrees of freedom in the fluid such that any heating does not change the temperature.

The 2<sup>nd</sup> order well-balanced MUSCL TVD scheme presented and extensively tested in Part I of this series will be used to solve (11). The implementation uses the van Leer flux limiter to maintain monotonicity and utilises the HLLC approximate Riemann solver with solution characteristics based on the state obtained from the Adaptive Noniterative Riemann Solver of Toro (1999). Finally the well-balanced correction of Käppeli and Mishra (2016) mitigates numerical artefacts arising from the typical source splitting near equilibrium. The advection and source terms are stepped forward unsplit using the 2<sup>nd</sup> order modified Runge-Kutta Strong Stability-Preserving scheme so as to inherit the TVD properties of the MUSCL scheme.

Each of  $\Delta$ ,  $\Phi_2$ , and  $\Omega$  are only implicit functions of  $t$ , and so the orbital location of the

shearing box,  $\varphi$ , must be determined as a function of time. This requires solving the ODE

$$\frac{d\varphi}{dt} = \Omega(\lambda_0, \varphi) = \sqrt{\frac{GM}{\lambda_0^3}} (1 + e \cos \theta)^2. \quad (12)$$

Alternatively, a more accurate solution can be obtained by using Kepler's method to determine the true anomaly as a function of time. This is found by directly computing

$$\theta(t) = 2 \tan^{-1} \left( \sqrt{\frac{1+e}{1-e}} \tan \left( \frac{\mathcal{E}}{2} \right) \right) \quad (13)$$

where the eccentric anomaly,  $\mathcal{E}$ , is first found by numerically solving

$$\frac{2\pi t}{\mathcal{P}} \bmod 2\pi = \mathcal{E} - e \sin \mathcal{E} \quad (14)$$

for example by using the Newton-Raphson method. Thus  $\varphi(t) = \theta + \omega$  can be quickly computed at each time step.

### 3.1 Boundary Conditions

A rigid (no-flux) boundary is enforced far from the largest expected scale height at apocentre, so as to prevent artificially restricting the disc expansion. This requires setting an isothermal equilibrium pressure gradient in the ghost cells corresponding to the gravitational potential at the particular orbital location. The hydrostatic pressure-reconstructive boundary conditions detailed in Part I are modified for the periodic effective potential. The pressure and density are extrapolated from the domain edge into the ghost zones corresponding to the equilibrium expected by the well-balanced solver.

It should be noted that this boundary condition does not preserve the form of the primitive variables in (7). This can generate a number of devastating numerical artefacts if left unmitigated. In particular, the no-penetration condition at the boundary produces a rarefaction wave proportional to the local density as the initial profile begins to collapse from apocentre. A reciprocal wave is also generated as the fluid expands again and collides against the rigid boundary. Setting the boundaries at  $z = \pm 8H_{\text{apo}}$  was found to sufficiently distance these artefacts from the centre profile of interest. The low density ( $1.2 \cdot 10^{-14}$ ) at the edges also helps to contain the waves and reduce the errors they cause.

### 3.2 Initial Conditions

The initial conditions at apocentre must be carefully chosen to produce only the forced response. This requires numerically solving the periodic boundary value problem (10) to determine the initial scale height at apocentre as well as the state defined by  $\hat{\rho}$ ,  $\hat{w}$ , and  $\hat{p}$ . A shooting method using 4<sup>th</sup> order Runge-Kutta integration is iterated until both  $H$  and  $\dot{H}$  are periodic to a tolerance of  $10^{-14}$ . The vertical velocity may then be found by central differencing and using  $\hat{w} = \dot{H}/H$ ; however, for the case of an isothermal disc, the solution is symmetric and  $\hat{w}_0 = 0$ . In either case, the density is floating and so  $\hat{\rho}_0 = 1.0$  is chosen. Finally, the temperature is chosen to put the tests in units of the isothermal scale height at  $r = \lambda_0$ . Thus  $c_s$  is defined such that each of  $H_{\text{iso}}$  and  $\Omega$  are unity at  $r = \lambda_0$ .

One difficulty that arises when the domain is very large relative to the scale height is that small perturbations — even on the order of machine precision — exponentially grow when propagated into the rarefied atmosphere (see §4.2.3 in Part I). For isentropic waves, small velocity perturbations at the midplane will amplify by an amount

$$\mathcal{A} = \exp \left( \frac{z^2}{2H^2} \right) \quad (15)$$

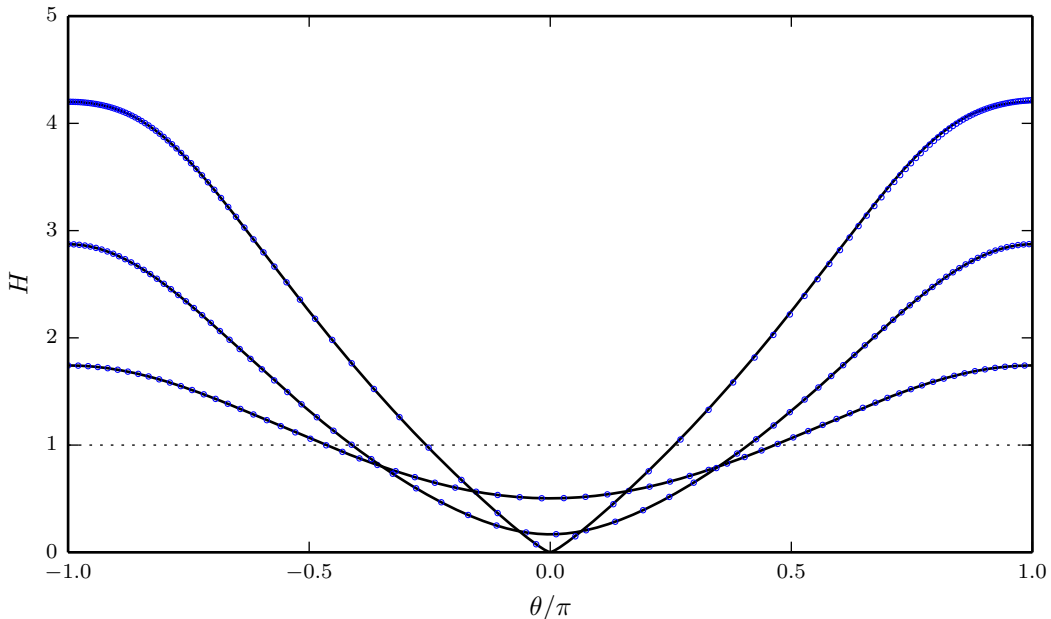


Figure 4: The scale height evolution in units of the hydrostatic scale height for a circular disc with  $R_0 = \lambda_0$ . Shown here over one orbit computed with the well-balanced MUSCL scheme using  $H_{\text{peri}}/\Delta z = 4.0$  for  $e = 0.2, 0.4,$  and  $0.6$ , and with each semi-analytic solution for reference.

which is just the inverse of the stratification scaling factor for an isothermal disc. Thus for  $L_z/H \gtrsim 17$ , machine precision errors dominate the velocity solution before reaching the boundaries, artificially suppressing  $\Delta t$ . A solution to mitigate this problem adds an artificial atmosphere analogous to the prescription common for adiabatic atmospheres beyond the adiabatic scale height. This involves enforcing a density floor of  $10^{-14}$ , and ensuring it is initially in hydrostatic balance. Although this is not applicable for the chosen domain size of  $L_z = 16H_{\text{apo}}$ , the artificial atmosphere must be implemented for testing with larger domains.

## 4 Results and Validation

The 1D well-balanced 2<sup>nd</sup> order MUSCL TVD scheme with a general nonlinear source term was extensively tested and validated in Part I of this series. The well-balanced property of the modified implementation described above was again ensured for the trivial hydrostatic case  $e = 0$ , which was verified to hold to machine precision. A range of eccentricities up to  $e = 0.6$  with  $e' = \omega' = 0$  were then evolved and compared to the forced response of the isothermal semi-analytic solution of §2.3. It was pointed out by Barker and Ogilvie (2014) that eccentric discs above  $e \sim 0.5$  are less dynamically interesting due to instigated shocks permeating the disc and quickly dissipating the eccentric mode on the dynamical timescale. Nonetheless, a disc with  $e = 0.6$  will be simulated to demonstrate the ability of the implemented finite volume methods at dealing with the extreme compression at pericentre.

The well-balanced MUSCL TVD scheme is initially compared between tests with  $e = 0.2, 0.4,$  and  $0.6$ . Each trial set a domain,  $L_z = 16H_{\text{apo}}$ , with the number of grid cells chosen such that  $H_{\text{peri}}/\Delta z = 4.0$ . This provided sufficient resolution to accurately capture the momentary extreme compression at pericentre (well exceeding  $p_{\text{peri}}/p_{\text{apo}} = 100$  when  $e = 0.6$ ), and rebound with a relative error less than 0.01 in the scale height. For  $e = 0.2$ , this requires only 250 cells. However, when  $e = 0.6$ , a domain size of  $L_z = 67.2$  is needed to accommodate  $H_{\text{apo}} = 4.2$ ,

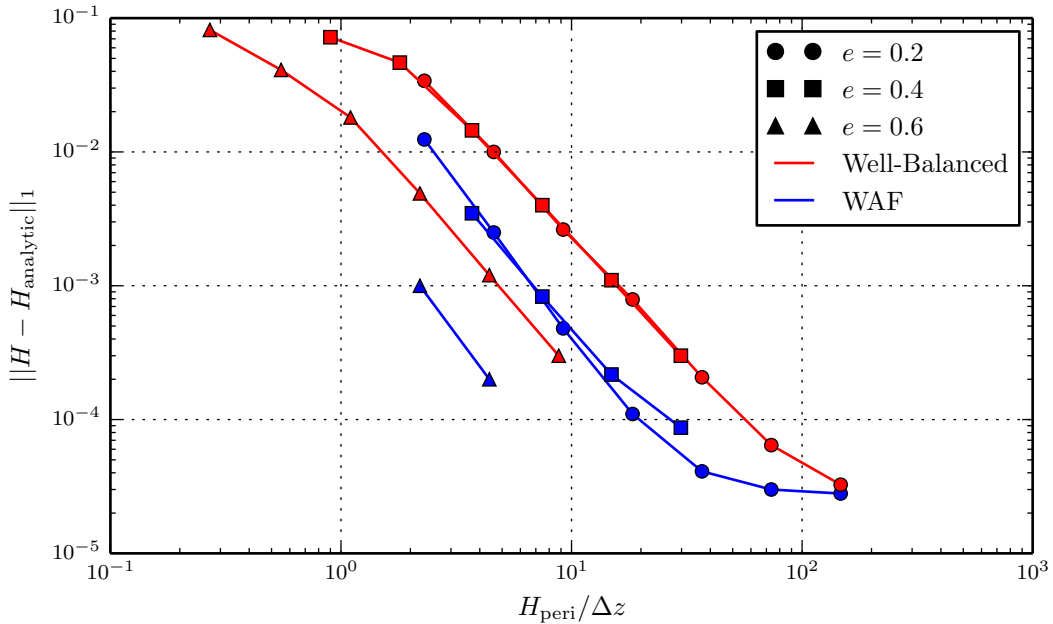


Figure 5: Convergence plot comparing the  $L_1$ -norm error in scale height for the MUSCL well-balanced scheme (red) and WAF scheme (blue).

while at the same time  $H_{\text{peri}} = 0.0026$ , thus requiring over  $10^5$  grid cells! These finite volume results are presented overlaid on the semi-analytic solution in Figure 4. The resultant error is not entirely dependent on  $H_{\text{peri}}/\Delta z$ , and decreases with increasing eccentricity likely due to the reduced residence time near pericentre for larger eccentricities.

A convergence study was then undertaken to compare the performance of the WAF and well-balanced MUSCL schemes. Although WAF appears to obtain slightly higher convergence, it fails to find a solution with fewer than about 2 cells per scale height. This is likely due to the inability to compute the extreme wave characteristics, but which nonetheless factor into the weighted solution because WAF utilises each solution state. It is quite computationally expensive then to compute the solutions for  $e = 0.6$  with more than 4 cells per scale height, which limits the extent of the  $e = 0.6$  convergence study. The well-balanced MUSCL scheme does obtain better accuracy for eccentricities  $e \lesssim 0.1$ , when the truncation errors from the unbalanced source and advection terms would dominate the WAF error.

As apparent in Figure 5, convergence is stalled for both schemes beyond an accuracy  $2 \cdot 10^{-5}$  by sources of error which do not decrease with increasing resolution. A main source of this error comes from the rarefaction wave initially generated at the boundary from the initial acceleration of the disc. This manifests as an increasing sinusoid in the error, at  $t \sim L_z/(2c_s)$ . As this system is very stiff near pericentre for large eccentricity, any small perturbations propagating from the boundaries (and positively reinforcing at the centre) increasingly produce errors in the final scale height measured at apocentre. The forced solution presented in §2.3 in the special case of an isothermal disc is also known to depend on  $\gamma$  for general thermodynamics (Ogilvie and Barker, 2014). Using  $\gamma = 1.001$ , as is the typical prescription for emulating isothermal thermodynamics, stalls convergence an order of magnitude sooner than when using  $\gamma = 1.00001$ . However, decreasing  $\gamma$  even more was not found to further decrease the error, likely because calculating the Riemann states with  $\gamma$  too close to 1.0 forms a very stiff problem. The only way to avoid this error source completely is then to reformulate the entire implementation specifically to solve the isothermal equations.

## 5 Conclusions and Future Work

The modifications to the finite volume methods developed in Part I of this series were presented with geometric sourcing terms accounting for disc eccentricity. Results were presented for a range of disc eccentricities, and it was found that for reasonable  $H_{\text{peri}}/\Delta z$ , each solver rebounds to the original scale height at apocentre to within an error of  $2 \cdot 10^{-5}$  per orbit. However, it is suspected that for even more extreme compressions than that experienced in  $e = 0.6$ , a stiff integration routine will be necessary due to the increasingly ill-conditioned nature with larger eccentricity.

Future work will lift the restriction of an aligned, constant eccentricity disc, generalising the numerics so that  $w' \neq 0$  and  $e' \neq 0$ . For this change to have any effect on the dynamical response, the fluid must not be isothermal. Thus a new method to eliminate the free oscillations must be developed because a semi-analytic solution is not possible for a general equation of state. This may be possible by implementing a minuscule viscous damping term to dissipate the extra energy stored in the free oscillation modes.

Finally, to attain further convergence, it has become apparent that a more representative boundary condition must be implemented in order to minimise artefacts generated at the ghost zones. An ideal boundary condition would maintain the form (7) of the primitive variables even into the ghost cells. Future work will explore various extrapolation methods, in particular using nonlinear gaussian regression for the pressure and density, and linear regression to extrapolate the vertical velocity. This would permit solution on a smaller domain without inhibiting the convergence by eliminating the rarefaction waves propagating inwards from the boundaries.

Future research will extend the eccentric shearing box implementation into 2D, including also the radial-like dimension, to explore the destabilisation of locally axisymmetric inertial wave modes.

## References

- A. J. Barker and G. I. Ogilvie. Hydrodynamic instability in eccentric astrophysical discs. *Monthly Notices of the Royal Astronomical Society*, 445(1):2637–2654, Sept. 2014.
- R. Käppeli and S. Mishra. A well-balanced finite volume scheme for the Euler equations with gravitation. *Astronomy and Astrophysics*, 587:A94, Feb. 2016.
- W. Kley and G. Dirksen. Disk eccentricity and embedded planets. *Astronomy and Astrophysics*, 447(1):369–377, Feb. 2006.
- D. N. C. Lin and J. E. Pringle. Numerical Simulation of Mass Transfer and Accretion Disc Flow in Binary Systems. In *Structure and Evolution of Close Binary Systems*, pages 237–252. Springer Netherlands, Dordrecht, 1976.
- S. H. Lubow. A model for tidally driven eccentric instabilities in fluid disks. *The Astrophysical Journal*, 381:259–267, Nov. 1991.
- S. H. Lubow. Eccentricity growth rates of tidally distorted discs. *Monthly Notices of the Royal Astronomical Society*, 406(1):2777–2786, May 2010.
- Y. E. Lyubarskij, K. A. Postnov, and M. E. Prokhorov. Eccentric accretion discs. *Monthly Notices of the Royal Astronomical Society*, 266(3):583–596, Feb. 1994.
- G. I. Ogilvie. Non-linear fluid dynamics of eccentric discs. *Monthly Notices of the Royal Astronomical Society*, 325(1):231–248, July 2001.
- G. I. Ogilvie and A. J. Barker. Local and global dynamics of eccentric astrophysical discs. *Monthly Notices of the Royal Astronomical Society*, 445(1):2621–2636, Sept. 2014.
- J. C. B. Papaloizou. The local instability of steady astrophysical flows with non circular streamlines with application to differentially rotating disks with free eccentricity. *Astronomy and Astrophysics*, 432(3):743–755, Mar. 2005.
- J. E. Pringle. Accretion Discs in Astrophysics. *Annual Review of Astronomy and Astrophysics*, 19(1):137–160, Sept. 1981.
- D. Syer and C. J. Clarke. The viscous evolution of elliptical accretion discs. *Monthly Notices of the Royal Astronomical Society*, 255(1):92–104, Mar. 1992.
- E. F. Toro. *Riemann Solvers and Numerical Methods for Fluid Dynamics*. Springer, Berlin, Heidelberg, 2 edition, 1999.
- R. Whitehurst. Numerical simulations of accretion discs – I. Superhumps: a tidal phenomenon of accretion discs. *Monthly Notices of the Royal Astronomical Society*, 232(1):35–51, May 1988.